Negative refraction using Raman transitions and chirality

D. E. Sikes and D. D. Yavuz

Department of Physics, 1150 University Avenue, University of Wisconsin at Madison, Madison, Wisconsin 53706, USA
(Received 22 August 2011; published 17 November 2011)

We present a scheme that achieves negative refraction with low absorption in far-off resonant atomic systems. The scheme utilizes Raman resonances and does not require the simultaneous presence of an electric-dipole transition and a magnetic-dipole transition near the same wavelength. We show that two interfering Raman transitions coupled to a magnetic-dipole transition can achieve a negative index of refraction with low absorption through magnetoelectric cross-coupling. We confirm the validity of the analytical results with exact numerical simulations of the density matrix. We also discuss possible experimental implementations of the scheme in rare-earth metal atomic systems.

The concept of negative refraction, which was first predicted by Veselago [1] more than four decades ago, has recently emerged as a very exciting field of science. In his seminal paper, Veselago argued that materials with simultaneously negative permittivity and permeability would acquire a negative index of refraction, $n < 0$ [1]. These materials exhibit many seemingly strange properties such as the electromagnetic vectors forming a left-handed triad (hence the term left-handed materials) and the Poynting vector being antiparallel to the k vector. Although the interest in these materials remained only a scientific curiosity for a long time, it is now understood that negative refraction may have important and far-reaching practical consequences. The key potential application for these materials was discovered in the year 2000 when Pendry predicted that a slab with a negative index of refraction, known as a perfect lens, can image objects with, in principle, unlimited resolution [2]. If experimentally demonstrated, perfect lenses may provide a unique technique for imaging nanoscale objects and may therefore have significant implications for a number of research areas. Since Pendry's suggestion, the interest in negative refraction has been continuously growing, and there have been a large number of exciting theoretical developments and experimental advances [3–20], including the observation of electromagnetic cloaking [21,22].

Materials with a negative index of refraction do not exist naturally, and thus they need to be artificially constructed. One approach is to artificially engineer periodic metal-dielectric structures with appropriate electric and magnetic resonances. These structures, termed metamaterials, typically have a characteristic periodicity scale smaller than the wavelength so that a nearly uniform electromagnetic response is obtained. Initial experiments have demonstrated negative refraction in the microwave region of the spectrum using metamaterials constructed from metal wires and split-ring resonators [5–9]. Recently, utilizing advances in nanolithography techniques, several groups have reported a negative index of refraction at optical frequencies in metal-dielectric nanostructures and photonic crystals [10–20]. A key difficulty of these experiments that is particularly pronounced in the optical domain is the large absorption that accompanies negative refraction. For all experiments that have been performed in the optical region of the spectrum, the imaginary part of the refractive

index is almost as large as the real part. This is a key limitation for many potential applications since light is largely absorbed within a few wavelengths of propagation inside the material.

In this paper, we focus on atomic systems that are driven with lasers in their internal states so that negative refraction for a weak probe wave is achieved. The key advantages of using driven atomic systems as opposed to metamaterials are (i) using interference principles, one can obtain a negative index of refraction with negligible absorption; (ii) atomic systems are uniquely suited for achieving negative refraction at shorter and shorter wavelengths, particularly in the visible and ultraviolet regions of the spectrum; (iii) since negative refraction is achieved through manipulation of internal states, the properties of the material can be dynamically modified, opening an array of exciting applications including perfect-lens switches. Despite these advantages, achieving negative refraction in atomic systems is a very challenging problem that has not yet been experimentally demonstrated due to several difficulties. All recent proposals require a strong electric-dipole transition and a strong magnetic-dipole transition at almost exactly the same wavelength. It is difficult to satisfy this condition in real atomic systems. Furthermore, achieving negative permittivity and permeability simultaneously requires atomic densities greater than 10^{18} cm^{-3}, which is impractical.

We have recently suggested an approach that overcomes some of these difficulties [23]. In this paper, we give a more detailed description of our approach, provide numerical calculations that confirm the validity of the analytical predictions, and present a preliminary assessment of possible experimental implementations in real atomic systems. As we detail below, our technique relies on the interference of two Raman transitions combined with magnetoelectric coupling (chirality). The key advantage of our approach is that it does not require the simultaneous presence of an electric-dipole transition and a magnetic-dipole transition near the same wavelength. This gives considerable flexibility in the energy-level structure and allows our technique to be implemented with a number of different atomic species. Furthermore, because of the chiral response, negative refraction does not require negative permeability and can be achieved at much lower atomic densities compared to nonchiral schemes.

I. BACKGROUND AND RELATION TO PREVIOUS WORK

As mentioned above, Veselago's original proposal for achieving a negative index of refraction requires $\epsilon < 0$ and $\mu < 0$ simultaneously. Using this idea, Oktel and Mustecapli-oglu [24] and Thommen and Mandel [25] were the first to study the possibility of negative refraction in driven atomic systems. In the optical region of the spectrum the chief difficulty of this approach is the weakness of the magnetic response. Since typical magnetic-dipole moments are weaker than electric-dipole moments, achieving negative permeability requires impractically large atomic densities. To alleviate this problem, a chiral route to negative refraction has recently been suggested [26,27]. Here, the key idea is to use a magnetoelectric cross-coupling where the medium's electric polarization is coupled to the magnetic field of the wave and the medium's magnetization is coupled to the electric field. As we discuss below, under such conditions, negative refraction can be achieved without requiring a negative permeability. Building on this idea, Walsworth and colleagues have recently suggested a promising scheme that achieves negative refraction with low absorption using quantum interference [28,29]. Their scheme utilizes the dark state of electromagnetically induced transparency (EIT) to reduce absorption while enhancing the chiral response. This scheme appears to be the most promising of the previously suggested approaches and achieves negative refraction with low loss at a density of about 5×10^{16} cm^{-3}.

All of the recent suggestions mentioned above require a strong magnetic-dipole transition and a strong electric-dipole transition at almost exactly the same wavelength. This requirement puts a stringent constraint on the energy-level structure of systems in which negative refraction can be achieved. Our approach [23] overcomes this constraint and furthermore achieves negative refraction with more conservative atomic system parameters (including atomic density and linewidth) compared to previous suggestions. We achieve these benefits at the expense of requiring two intense control lasers. Together with the probe laser, these control lasers induce two Raman transitions: one absorptive and one amplifying in nature. The interference of these two transitions results in a strong enhancement of the permittivity while minimizing absorption. We then coherently couple to a magnetic-dipole transition to obtain a chiral response and to achieve a negative index of refraction through magnetoelectric cross-coupling.

Our work should be viewed as part of a broad class of techniques that focus on modifying the optical properties of an atomic medium. Over the last two decades, there have been exciting advances in this field. It is now understood that, by using EIT and similar techniques [30–33], one can obtain slow light [34–38] and stopped light [39–43], and one can construct optical nonlinearities that are large enough to be effective at the single-photon level [44–54]. Observation of these effects has opened up a number of exciting applications in various research areas including photonic quantum computation and all-optical data processing. The key difference of our work is that our goal is to modify the value of the refractive index, whereas EIT and similar techniques typically utilize the steep dispersion (the slope) of the refractive index as a function of frequency.

Before proceeding with a detailed description of our suggestion, we summarize the chiral approach to negative

refraction. Consider a probe beam with electric-field and magnetic-field components $\mathcal{E}_p$ and $\mathcal{B}_p$, respectively. In a material with magnetoelectric cross-coupling, the medium polarization, P_p, and the magnetization, M_p, are given by [28,29]

$$P_p = \epsilon_0 \chi_\mathcal{E} \mathcal{E}_p + \frac{\xi_{\mathcal{E}\mathcal{B}}}{c\mu_0} \mathcal{B}_p,$$
$$M_p = \frac{\xi_{\mathcal{B}\mathcal{E}}}{c\mu_0} \mathcal{E}_p + \frac{\chi_\mathcal{B}}{\mu_0} \mathcal{B}_p, \tag{1}$$

where $\chi_\mathcal{E}$ and $\chi_\mathcal{B}$ are the electric and magnetic susceptibilities and $\xi_{\mathcal{E}\mathcal{B}}$ and $\xi_{\mathcal{B}\mathcal{E}}$ are the complex magnetoelectric coupling (chirality) coefficients, respectively. The index of refraction of the medium for a plane wave of a particular circular polarization can be found by using Eqs. (1) and Maxwell's equations:

$$n = \sqrt{\epsilon\mu - \frac{(\xi_{\mathcal{E}\mathcal{B}} + \xi_{\mathcal{B}\mathcal{E}})^2}{4}} + \frac{i}{2}(\xi_{\mathcal{E}\mathcal{B}} - \xi_{\mathcal{B}\mathcal{E}}). \tag{2}$$

Here, $\epsilon = 1 + \chi_\mathcal{E}$ and $\mu = 1 + \chi_\mathcal{B}$ are the relative permittivity and permeability of the medium. As shown in Eq. (2), the chirality coefficients result in additional contributions to the index of refraction. The key idea behind the chiral approach is that, in the optical region, one typically has the scaling $\chi_\mathcal{B} \sim \alpha^2 \chi_\mathcal{E}$ and $(\xi_{\mathcal{E}\mathcal{B}}, \xi_{\mathcal{B}\mathcal{E}}) \sim \alpha \chi_\mathcal{E}$, where $\alpha \approx 1/137$ is the fine structure constant. Since the values of the chirality coefficients are smaller only by a factor of α instead of α^2, negative refraction can be achieved without the need for negative permeability and at much smaller atomic densities compared to nonchiral schemes. Negative refraction with chirality requires appropriate phase control of the chirality coefficients which can be achieved through coherent magnetoelectric coupling. One typically chooses the phase such that the chirality coefficients are imaginary, $\xi_{\mathcal{E}\mathcal{B}} = -\xi_{\mathcal{B}\mathcal{E}} = i\xi$, and Eq. (2) reads $n = \sqrt{\epsilon\mu} - \xi$. Achieving $n < 0$ then requires a sufficiently large chiral response such that $\xi > \sqrt{\epsilon\mu}$. Furthermore, to reduce absorption, it is critical to keep the imaginary part of the refractive index to be as low as possible. The performance of negative index materials is typically characterized by the figure of merit, $F_M = -\text{Re}(n)/|\text{Im}(n)|$.

II. NEGATIVE REFRACTION USING RAMAN TRANSITIONS WITH CROSS-COUPLING

We proceed with a detailed description of our suggestion. Noting Fig. 1, we consider a six-level system interacting with four laser beams. We wish to achieve a negative index of refraction for the probe laser beam with field components $\mathcal{E}_p$ and $\mathcal{B}_p$, respectively. We take the atomic system to have a strong magnetic transition with dipole-moment μ_{gm} near the frequency of the probe laser beam. As mentioned above, the system does not have a strong electric-dipole transition near the probe laser frequency. The electric-dipole response is obtained by using two-photon Raman transitions through the excited states $|a\rangle$ and $|b\rangle$. At the heart of the scheme is the recently predicted and experimentally demonstrated "refractive index enhancement with vanishing absorption" technique [55–58]. This technique was motivated by the pioneering efforts of Scully and others on index enhancement using quantum coherence [59–63]. Starting with the ground state $|g\rangle$, we induce two Raman transitions using the probe laser and two
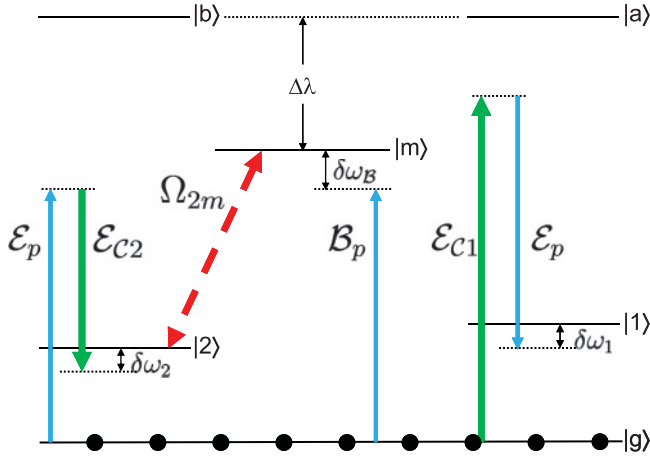
FIG. 1. (Color online) Schematic of the proposed scheme. $\mathcal{E}_p$ and $\mathcal{B}_p$ are the electric-field and magnetic-field components of a weak far-off resonant probe beam (thin blue arrow). $|g\rangle \rightarrow |m\rangle$ is a magnetic-dipole transition induced by the probe magnetic field $\mathcal{B}_p$. Two strong control lasers (thick green arrow), $\mathcal{E}_{C1}$ and $\mathcal{E}_{C2}$, induce two electric-dipole Raman transitions for the probe beam. The Raman transitions can be far-detuned from the excited states $|a\rangle$ and $|b\rangle$. Therefore, the system does not require the magnetic ($|g\rangle \rightarrow |m\rangle$) and electric ($|g\rangle \rightarrow |a\rangle$ and $|g\rangle \rightarrow |b\rangle$) transitions to be near the same frequency. Ω_{2m} (red dashed arrow) induces magnetoelectric cross-coupling (chirality).

intense control lasers with electric-field amplitudes $\mathcal{E}_{C1}$ and $\mathcal{E}_{C2}$. Since the order at which the probe laser beam is involved in each Raman transition is different, this scheme achieves two resonances: one amplifying and one absorptive in nature. The strength and position of these two resonances can be controlled by varying the intensities and frequencies of the control laser beams. It is the interference of these two resonances that results in the control of the index of refraction while maintaining small absorption. The magnetoelectric cross-coupling is achieved through coherent coupling of states $|2\rangle$ and $|m\rangle$ with a separate laser beam of Rabi frequency Ω_{2m}. States $|g\rangle$, $|1\rangle$, $|2\rangle$, and $|m\rangle$ have the same parity, which is opposite to the parity of states $|a\rangle$ and $|b\rangle$. Since states $|2\rangle$ and $|m\rangle$ have the same parity, the coherent coupling Ω_{2m} cannot be electric-dipole, but instead can be achieved through the magnetic field of a strong laser or through a separate two-photon transition (not shown). The two-photon detunings from the two Raman transitions are defined as: $\delta\omega_1 = (\omega_1 - \omega_g) - (\omega_{C1} - \omega_p)$ and $\delta\omega_2 = (\omega_2 - \omega_g) - (\omega_p - \omega_{C2})$. The quantity $\delta\omega_\mathcal{B} = (\omega_m - \omega_g) - \omega_p$ is the detuning of the probe laser beam from the $|g\rangle \rightarrow |m\rangle$ magnetic transition.

Without loss of generality, we have chosen the probe fields $\mathcal{E}_p$ and $\mathcal{B}_p$ to have σ_+ polarization while the coupling fields Ω_{2m}, $\mathcal{E}_{C1}$, and $\mathcal{E}_{C2}$ have σ_- polarization. These circular polarized fields interact within the Zeeman sublevel structure of the atom. For a system where the particular fields are oppositely circular polarized, we would expect the terms in Eq. (2) to interfere differently, which could lead to an enhanced positive index of refraction. For a linear polarization of the fields we would expect the medium to exhibit unusually high optical rotation of the probe beam.

We start by expanding the total wave function for the atomic system, $|\psi\rangle$, in the interaction picture:

$$
\begin{aligned}
|\psi\rangle = &\, c_g \exp(-i\omega_g t)|g\rangle + c_1 \exp(-i\omega_1 t)|1\rangle \\
&+ c_2 \exp(-i\omega_2 t)|2\rangle + c_m \exp(-i\omega_m t)|m\rangle \\
&+ c_a \exp(-i\omega_a t)|a\rangle + c_b \exp(-i\omega_b t)|b\rangle,
\end{aligned}
\tag{3}
$$

where the quantities c_i are the complex probability amplitudes of the respective levels. The total Hamiltonian of the system can be written as $\hat{H}_{\text{total}} = \hat{H}_0 + \hat{H}_{\text{int}}$, where $\hat{H}_0$ is the unperturbed Hamiltonian and $\hat{H}_{\text{int}}$ is the interaction Hamiltonian that includes the interactions of the atom with the electric-field and magnetic-field components of the incident waves:

$$
\begin{aligned}
\hat{H}_0 = &\, \hbar\omega_g|g\rangle\langle g| + \hbar\omega_1|1\rangle\langle 1| + \hbar\omega_2|2\rangle\langle 2| + \hbar\omega_m|m\rangle\langle m| \\
&+ \hbar\omega_a|a\rangle\langle a| + \hbar\omega_b|b\rangle\langle b|, \\
\hat{H}_{\text{int}} = &\, -d_{ga}\mathcal{E}|g\rangle\langle a| - d_{gb}\mathcal{E}|g\rangle\langle b| - d_{1a}\mathcal{E}|1\rangle\langle a| - d_{2b}\mathcal{E}|2\rangle\langle b| \\
&- \mu_{gm}\mathcal{B}|g\rangle\langle m| - \mu_{2m}\mathcal{B}|2\rangle\langle m| + \text{H.c.}
\end{aligned}
\tag{4}
$$

Here, the quantities d_{ij} and μ_{ij} are the electric-dipole and magnetic-dipole transition matrix elements between respective levels, $\mathcal{E}$ and $\mathcal{B}$ are the total electric and magnetic fields, and H.c. refers to the Hermitian conjugate. The electric and magnetic fields include contributions from all relevant laser beams and they are

$$
\begin{aligned}
\mathcal{E} = &\, \text{Re}\{\mathcal{E}_p \exp(-i\omega_p t) + \mathcal{E}_{C1} \exp(-i\omega_{C1} t) \\
&+ \mathcal{E}_{C2} \exp(-i\omega_{C2} t)\}, \\
\mathcal{B} = &\, \text{Re}\{\mathcal{B}_p \exp(-i\omega_p t) + \mathcal{B}_{2m} \exp(-i\omega_{2m} t)\}.
\end{aligned}
\tag{5}
$$

In the above equations, for concreteness, we have taken the magnetoelectric cross-coupling to be induced by a third intense laser beam with magnetic field $\mathcal{B}_{2m}$. Using Eqs. (3) and (4) and ignoring the dissipative processes for the moment, we write the Schrödinger's equation for the time evolution of the probability amplitudes:

$$
\begin{aligned}
\dot{c}_g = &\, \frac{i}{\hbar}\{d_{ga}\mathcal{E}c_a \exp[i(\omega_g - \omega_a)t] + d_{gb}\mathcal{E}c_b \exp[i(\omega_g - \omega_b)t] \\
&+ \mu_{gm}\mathcal{B}c_m \exp[i(\omega_g - \omega_m)t]\}, \\
\dot{c}_1 = &\, \frac{i}{\hbar}\{d_{1a}\mathcal{E}c_a \exp[i(\omega_1 - \omega_a)t]\}, \\
\dot{c}_2 = &\, \frac{i}{\hbar}\{d_{2b}\mathcal{E}c_b \exp[i(\omega_2 - \omega_b)t] + \mu_{2m}\mathcal{B}c_m \exp[i(\omega_2 - \omega_m)t]\}, \\
\dot{c}_m = &\, \frac{i}{\hbar}\{\mu_{gm}^*\mathcal{B}c_g \exp[i(\omega_m - \omega_g)t] \\
&+ \mu_{2m}^*\mathcal{B}c_2 \exp[i(\omega_m - \omega_2)t]\}, \\
\dot{c}_a = &\, \frac{i}{\hbar}\{d_{1a}^*\mathcal{E}c_1 \exp[i(\omega_a - \omega_1)t] + d_{ga}^*\mathcal{E}c_g \exp[i(\omega_a - \omega_g)t]\}, \\
\dot{c}_b = &\, \frac{i}{\hbar}\{d_{2b}^*\mathcal{E}c_2 \exp[i(\omega_b - \omega_2)t] + d_{gb}^*\mathcal{E}c_g \exp[i(\omega_b - \omega_g)t]\}.
\end{aligned}
\tag{6}
$$

Throughout this work, we focus on the case where the single-photon detunings from the excited electronic states are much larger than the coupling rates. This allows adiabatic elimination of the probability amplitudes of the excited electronic levels $|a\rangle$ and $|b\rangle$. This is an important simplification

for the analytical results since it reduces the problem to an effective four-level system. We note, however, that we do not make this simplification in the numerical results of the next section and solve the density matrix for the full six levels. As we discuss, the numerical results for the full system are in reasonable agreement with the analytical solutions. We take all the relevant detunings to be small compared to the absolute laser frequencies and make the rotating wave approximation. Integrating out the differential equations for c_a and c_b we obtain

$$c_a = \frac{d_{1a}^*}{2\hbar}c_1 \sum_{q=p,\mathcal{C}1,\mathcal{C}2} \frac{\mathcal{E}_q \exp[i(\omega_a - \omega_1 - \omega_q)t]}{\omega_a - \omega_1 - \omega_q} + \frac{d_{ga}^*}{2\hbar}c_g \sum_{q=p,\mathcal{C}1,\mathcal{C}2} \frac{\mathcal{E}_q \exp[i(\omega_a - \omega_g - \omega_q)t]}{\omega_a - \omega_g - \omega_q},$$

$$c_b = \frac{d_{2b}^*}{2\hbar}c_2 \sum_{q=p,\mathcal{C}1,\mathcal{C}2} \frac{\mathcal{E}_q \exp[i(\omega_b - \omega_2 - \omega_q)t]}{\omega_b - \omega_2 - \omega_q} + \frac{d_{gb}^*}{2\hbar}c_g \sum_{q=p,\mathcal{C}1,\mathcal{C}2} \frac{\mathcal{E}_q \exp[i(\omega_b - \omega_g - \omega_q)t]}{\omega_b - \omega_g - \omega_q}. \tag{7}$$

Using the algebraic expressions for the probability amplitudes of Eq. (7), the Schrödinger's equation for the simplified four level system is

$$\dot{c}_g + \frac{\mathrm{Im}(A)}{2}c_g = i\frac{B_1}{2}c_1 + i\frac{B_2}{2}c_2 + i\frac{\Omega_{gm}}{2}c_m, \quad \dot{c}_1 + i\left[\delta\omega_1 - \frac{\mathrm{Re}(F_1 - A)}{2}\right]c_1 + \left[\gamma_1 + \frac{\mathrm{Im}(F_1)}{2}\right]c_1 = i\frac{B_1^*}{2}c_g,$$

$$\dot{c}_2 + i\left[\delta\omega_2 - \frac{\mathrm{Re}(F_2 - A)}{2}\right]c_2 + \left[\gamma_2 + \frac{\mathrm{Im}(F_2)}{2}\right]c_2 = i\frac{B_2^*}{2}c_g + i\frac{\Omega_{2m}}{2}c_m,$$

$$\dot{c}_m + i\left[\delta\omega_\mathcal{B} + \frac{\mathrm{Re}(A)}{2}\right]c_m + \gamma_m c_m = i\frac{\Omega_{gm}^*}{2}c_g + i\frac{\Omega_{2m}^*}{2}c_2. \tag{8}$$

Here, we have added the decay rates of the levels, γ_1, γ_2, and γ_m, phenomenologically. At this stage of the formalism, since we are not using the density matrix, the decay processes are assumed to be to states outside the system. $\Omega_{gm} = \mu_{gm}\mathcal{B}_p^*/\hbar$ is the Rabi frequency due to magnetic field of the probe laser beam that couples states $|g\rangle$ and $|m\rangle$. $\Omega_{2m} = \mu_{2m}\mathcal{B}_{2m}^*/\hbar$ is the magnetoelectric cross-coupling rate. The quantities that appear in Eq. (8), within the rotating wave approximation, are given by

$$A = \mathrm{a}_p|\mathcal{E}_p|^2 + \mathrm{a}_{\mathcal{C}1}|\mathcal{E}_{\mathcal{C}1}|^2, \quad B_1 = b_1\mathcal{E}_p\mathcal{E}_{\mathcal{C}1}^*, \quad B_2 = b_2\mathcal{E}_p^*\mathcal{E}_{\mathcal{C}2}, \quad F_1 = f_{1,p}|\mathcal{E}_p|^2, \quad F_2 = f_{2,\mathcal{C}2}|\mathcal{E}_{\mathcal{C}2}|^2,$$

$$\mathrm{a}_p = \frac{1}{2\hbar^2}\left[\frac{|d_{gb}|^2}{\omega_b - \omega_g - \omega_p - i\Gamma_b}\right], \quad \mathrm{a}_{\mathcal{C}1} = \frac{1}{2\hbar^2}\left[\frac{|d_{ga}|^2}{\omega_a - \omega_g - \omega_{\mathcal{C}1} - i\Gamma_a}\right], \quad b_1 = \frac{1}{2\hbar^2}\left[\frac{d_{ga}d_{1a}^*}{\omega_a - \omega_g - \omega_{\mathcal{C}1} - i\Gamma_a}\right],$$

$$b_2 = \frac{1}{2\hbar^2}\left[\frac{d_{gb}d_{2b}^*}{\omega_b - \omega_g - \omega_p - i\Gamma_b}\right], \quad f_{1,p} = \frac{1}{2\hbar^2}\left[\frac{|d_{1a}|^2}{\omega_a - \omega_1 - \omega_p - i\Gamma_a}\right], \quad f_{2,\mathcal{C}2} = \frac{1}{2\hbar^2}\left[\frac{|d_{2b}|^2}{\omega_b - \omega_2 - \omega_{\mathcal{C}2} - i\Gamma_b}\right]. \tag{9}$$

Here, the quantities Γ_a and Γ_b are the decay rates of the excited levels $|a\rangle$ and $|b\rangle$, respectively.

III. ANALYTICAL STEADY-STATE SOLUTIONS

We proceed with a perturbative, steady-state analytical solution for the system. For this purpose, we take the laser intensities to be sufficiently weak such that most of the population stays in the ground atomic state, $c_g \approx 1$. For time scales that are long when compared with the inverse of the decay rates, the steady-state solutions for the probability amplitudes of the relevant levels are

$$c_1 \approx \frac{B_1^*}{2\left[\delta\omega_1 - \frac{\mathrm{Re}(F_1 - A)}{2} - i\left(\gamma_1 + \frac{\mathrm{Im}(F_1)}{2}\right)\right]}, \quad c_2 \approx \frac{2B_2^*\left[\delta\omega_\mathcal{B} + \frac{\mathrm{Re}(A)}{2} - i\gamma_m\right] + \Omega_{2m}\Omega_{gm}^*}{4\left[\delta\omega_2 - \frac{\mathrm{Re}(F_2 - A) - i\left(\gamma_2 + \frac{\mathrm{Im}(F_2)}{2}\right)}{2}\right]\left[\delta\omega_\mathcal{B} + \frac{\mathrm{Re}(A)}{2} - i\gamma_m\right] - |\Omega_{2m}|^2},$$

$$c_m \approx \frac{\Omega_{gm}^*}{2\left[\delta\omega_\mathcal{B} + \frac{\mathrm{Re}(A)}{2} - i\gamma_m\right]} + \frac{B_2^*\Omega_{2m}^*}{4\left[\delta\omega_\mathcal{B} + \frac{\mathrm{Re}(A)}{2} - i\gamma_m\right]\left[\delta\omega_2 - \frac{\mathrm{Re}(F_2 - A)}{2} - \frac{|\Omega_{2m}|^2}{4\left(\delta\omega_\mathcal{B} + \frac{\mathrm{Re}(A)}{2} - i\gamma_m\right)} - i\left(\gamma_2 + \frac{\mathrm{Im}(F_2)}{2}\right)\right]}$$

$$+ \frac{|\Omega_{2m}|^2\Omega_{gm}^*}{8\left[\delta\omega_\mathcal{B} + \frac{\mathrm{Re}(A)}{2} - i\gamma_m\right]^2\left[\delta\omega_2 - \frac{\mathrm{Re}(F_2 - A)}{2} - \frac{|\Omega_{2m}|^2}{4\left(\delta\omega_\mathcal{B} + \frac{\mathrm{Re}(A)}{2} - i\gamma_m\right)} - i\left(\gamma_2 + \frac{\mathrm{Im}(F_2)}{2}\right)\right]}. \tag{10}$$

As we discuss in the next section, we verify the validity of this steady-state solution by using full numerical simulations of the density matrix. With the analytical solutions for the probability amplitudes, we form coherences and calculate the medium's response at the probe laser frequency. The polarization and the magnetization of the medium are

$$P_p = 2\hbar N(\mathrm{a}_p|c_g|^2\mathcal{E}_p + b_1^*c_gc_1^*\mathcal{E}_{\mathcal{C}1} + b_2c_g^*c_2\mathcal{E}_{\mathcal{C}2}) \equiv N(\alpha_{\mathcal{E}\mathcal{E}}\mathcal{E}_p + \alpha_{\mathcal{E}\mathcal{B}}\mathcal{B}_p), \quad M_p = 2Nc_g^*c_m\mu_{gm} \equiv N(\alpha_{\mathcal{B}\mathcal{E}}\mathcal{E}_p + \alpha_{\mathcal{B}\mathcal{B}}\mathcal{B}_p), \tag{11}$$

where N is the number of atoms per unit volume. In the expressions above, the quantities $\alpha_{\mathcal{EE}}$, $\alpha_{\mathcal{BB}}$, $\alpha_{\mathcal{EB}}$, and $\alpha_{\mathcal{BE}}$ are the electric, magnetic, and cross-coupling polarizabilities and they are given by

$$\alpha_{\mathcal{EE}} = 2\hbar a_p + \frac{\hbar |b_1|^2 |\mathcal{E}_{\mathcal{C}1}|^2}{\left[\delta\tilde{\omega}_1 + i\left(\gamma_1 + \frac{\mathrm{Im}(F_1)}{2}\right)\right]} + \frac{\hbar |b_2|^2 |\mathcal{E}_{\mathcal{C}2}|^2}{\left[\delta\tilde{\omega}_2 - \frac{|\Omega_{2m}|^2}{4(\delta\tilde{\omega}_{\mathcal{B}} - i\gamma_m)} - i\left(\gamma_2 + \frac{\mathrm{Im}(F_2)}{2}\right)\right]}, \quad \alpha_{\mathcal{BB}} = \frac{|\mu_{gm}|^2}{\hbar\left[(\delta\tilde{\omega}_{\mathcal{B}} - i\gamma_m) - \frac{|\Omega_{2m}|^2}{4\left[\delta\tilde{\omega}_2 - i\left(\gamma_2 + \frac{\mathrm{Im}(F_2)}{2}\right)\right]}\right]},$$

$$\alpha_{\mathcal{EB}} = \frac{b_2 \mu_{gm}^* \mathcal{E}_{\mathcal{C}2} \Omega_{2m}}{2(\delta\tilde{\omega}_{\mathcal{B}} - i\gamma_m)\left[\delta\tilde{\omega}_2 - \frac{|\Omega_{2m}|^2}{4(\delta\tilde{\omega}_{\mathcal{B}} - i\gamma_m)} - i\left(\gamma_2 + \frac{\mathrm{Im}(F_2)}{2}\right)\right]}, \quad \alpha_{\mathcal{BE}} = \frac{b_2^* \mu_{gm} \mathcal{E}_{\mathcal{C}2}^* \Omega_{2m}^*}{2(\delta\tilde{\omega}_{\mathcal{B}} - i\gamma_m)\left[\delta\tilde{\omega}_2 - \frac{|\Omega_{2m}|^2}{4(\delta\tilde{\omega}_{\mathcal{B}} - i\Gamma_m)} - i\left(\gamma_2 + \frac{\mathrm{Im}(F_2)}{2}\right)\right]},$$

$$(12)$$

where we have introduced a simplified notation for the detunings that includes the ac Stark shifts:

$$\delta\tilde{\omega}_{\mathcal{B}} = \delta\omega_{\mathcal{B}} + \frac{\mathrm{Re}(A)}{2}, \quad \delta\tilde{\omega}_1 = \delta\omega_1 - \frac{\mathrm{Re}(F_1 - A)}{2},$$

$$\delta\tilde{\omega}_2 = \delta\omega_2 - \frac{\mathrm{Re}(F_2 - A)}{2}. \quad (13)$$

It is well-known that when the refractive index is strongly modified, the microscopic local fields can be substantially different than the averaged macroscopic fields. To calculate the susceptibilities, the chirality coefficients, and the refractive index, we include both electric and magnetic Clausius-Mossotti-type local-field effects [64,65]. For electric and magnetic fields, the relationships between microscopic local fields and macroscopic quantities are

$$\mathcal{E}_p^{\mathrm{micro}} = \mathcal{E}_p + \frac{1}{3\epsilon_0} P_p,$$

$$\mathcal{B}_p^{\mathrm{micro}} = \mathcal{B}_p + \frac{\mu_0}{3} M_p. \quad (14)$$

Solving Eq. (11) together with the local-field corrections of Eq. (14), we get the following expressions for the electric and magnetic susceptibilities and the chirality coefficients:

$$\chi_{\mathcal{E}} = N\frac{1}{\kappa\epsilon_0}\left[\alpha_{\mathcal{EE}} + N\frac{\mu_0}{3}(\alpha_{\mathcal{EB}}\alpha_{\mathcal{BE}} - \alpha_{\mathcal{EE}}\alpha_{\mathcal{BB}})\right],$$

$$\chi_{\mathcal{B}} = N\frac{\mu_0}{\kappa}\left[\alpha_{\mathcal{BB}} + N\frac{1}{3\epsilon_0}(\alpha_{\mathcal{EB}}\alpha_{\mathcal{BE}} - \alpha_{\mathcal{EE}}\alpha_{\mathcal{BB}})\right], \quad (15)$$

$$\xi_{\mathcal{EB}} = N\frac{\mu_0 c}{\kappa}\alpha_{\mathcal{EB}}, \quad \xi_{\mathcal{BE}} = N\frac{\mu_0 c}{\kappa}\alpha_{\mathcal{BE}},$$

where the quantity κ largely determines the density-dependent local-field enhancement and is

$$\kappa = 1 - N\frac{1}{3\epsilon_0}\alpha_{\mathcal{EE}} - N\frac{\mu_0}{3}\alpha_{\mathcal{BB}}$$

$$- N^2\frac{\mu_0}{9\epsilon_0}[\alpha_{\mathcal{EB}}\alpha_{\mathcal{BE}} - \alpha_{\mathcal{EE}}\alpha_{\mathcal{BB}}]. \quad (16)$$

Equations (11)–(16) represent the final results of this section. Given a certain set of parameters for our system such as matrix elements, laser intensities, and the atomic density, we use these equations to calculate the susceptibilities and the chirality coefficients. It is important to note that these equations are valid in the perturbative limit which will break down for sufficiently intense control laser beams. With the susceptibilities and chirality coefficients known, we then use Eq. (2) to calculate the real and imaginary parts of the refractive index.

IV. RESULTS FOR A MODEL ATOMIC SYSTEM

In this section we present results for a model atomic system. For this purpose, we consider a probe beam at a wavelength of $\lambda_p = 500$ nm. We assume the ideal case of pure radiative broadening for the excited electronic levels $|a\rangle$ and $b\rangle$ and take the radiative decay rates of these states to be $\Gamma_a = \Gamma_b = 2\pi \times 14.3$ MHz. The dipole matrix elements, d_{ia} and d_{ib} are calculated using the Wigner-Weisskopf result and assuming equal branching ratios, $d_{ia} = \sqrt{\pi\epsilon_0\Gamma_a\hbar c^3/\omega_p^3}$ and $d_{ib} = \sqrt{\pi\epsilon_0\Gamma_b\hbar c^3/\omega_p^3}$. We apply a similar procedure and assume a radiative decay rate of $\alpha^2\Gamma_a$ for the magnetic level $|m\rangle$ and calculate the corresponding magnetic-dipole matrix element, μ_{gm}. To simulate a realistic system, we assume an additional broadening mechanism (collisions, for example) with a rate $\gamma_c = 2\pi \times 1$ MHz and add this broadening to the linewidths of states $|1\rangle$, $|2\rangle$, and $|m\rangle$. We take the wavelengths of electric-dipole ($|g\rangle \to |a\rangle, |b\rangle$) and magnetic-dipole ($|g\rangle \to |m\rangle$) transitions to be different by $\Delta\lambda = 0.1$ nm. As we discuss below, this difference can be larger at the expense of an increase in the required control laser intensities. We take the magnetoelectric coupling laser beam to be resonant with the $|2\rangle \to |m\rangle$ transition and therefore take $\delta\tilde{\omega}_{\mathcal{B}} = \delta\tilde{\omega}_2$.

Figure 2 shows the susceptibilities and the chirality coefficients, $\chi_{\mathcal{E}}$, $\chi_{\mathcal{B}}$, $\xi_{\mathcal{EB}}$, and $\xi_{\mathcal{BE}}$, *without* the local-field corrections as the frequency of the probe laser beam is varied for an atomic density of $N = 5 \times 10^{16}$ cm^{-3}. Here, we assume that the control laser frequencies are appropriately adjusted such that the two Raman resonance frequencies coincide as the probe laser frequency is scanned, $\delta\tilde{\omega}_1 = -\delta\tilde{\omega}_2$. We take the intensities of the two control laser beams to be $I_{\mathcal{C}1} = 0.27$ MW/cm^2 and $I_{\mathcal{C}2} = 1.00$ MW/cm^2 and assume $\Omega_{2m} = i2\pi \times 1.36$ MHz. The intensities of the control lasers are adjusted to these values to have near cancellation of absorption. As shown in Fig. 2, the magneto-electric coupling causes an EIT-like level splitting for $\chi_{\mathcal{E}}$. The imaginary part of $\chi_{\mathcal{E}}$ becomes small near $\delta\tilde{\omega}_{\mathcal{B}} = 0$ due to the interference of the two Raman resonances. One of the key differences of our approach compared to the scheme of Fleischhauer *et al.* [28,29] is that since the electric-dipole response is due to Raman transitions, its strength is controlled by the intensity of the control laser beams. As a result, we do not have the usual scaling $\chi_{\mathcal{B}} \sim \alpha^2\chi_{\mathcal{E}}$ and $(\xi_{\mathcal{EB}}, \xi_{\mathcal{BE}}) \sim \alpha\chi_{\mathcal{E}}$, and
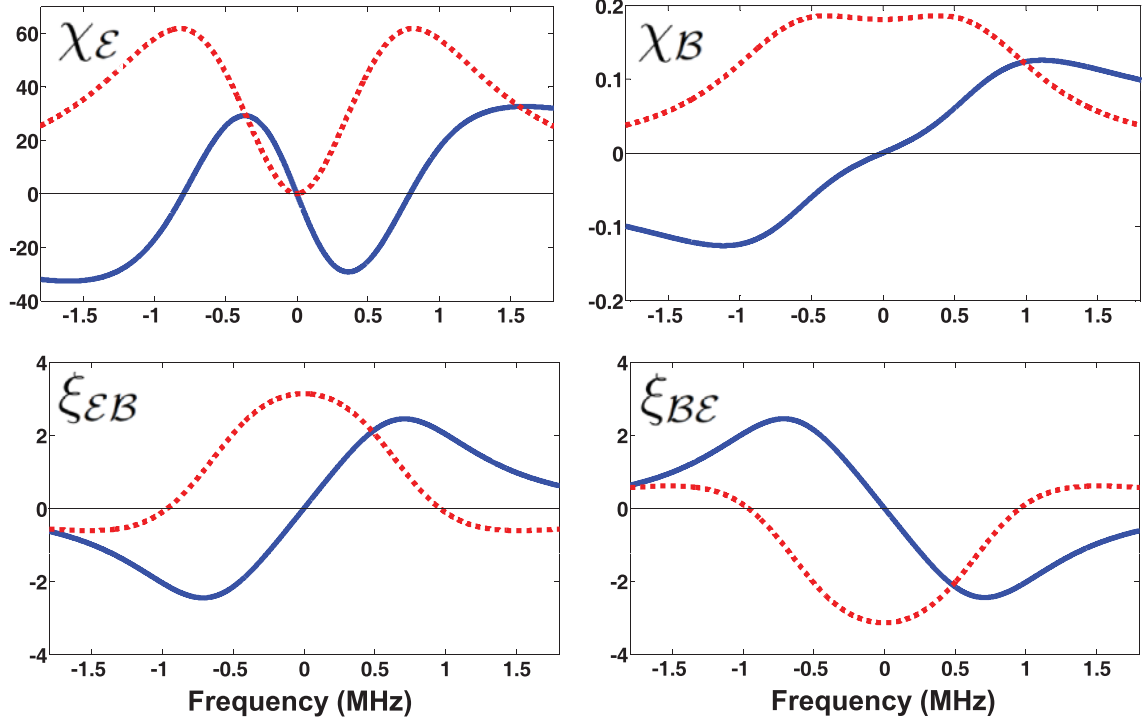
FIG. 2. (Color online) The real (solid blue line) and imaginary (dotted red line) parts of the susceptibilities and the chirality coefficients without the local-field corrections. See text for parameters. Since the electric-dipole response is due to Raman transitions, its strength is controlled by the intensity of the control laser beams. As a result, compared to earlier suggested schemes, the magnitude of $\chi_{\mathcal{E}}$ is more comparable to the chirality coefficients in our approach.

the magnitude of $\chi_{\mathcal{E}}$ can be made more comparable to the chirality coefficients.

Noting Eqs. (15) and (16), there is a strong density-dependent enhancement of both the electric and magnetic susceptibilities and the chirality coefficients. For sufficiently high densities, the local-field effects cause an enhancement of a susceptibility resonance and a shift of its frequency position [65]. Figure 3 shows the real and imaginary parts of the refractive index as the probe frequency is scanned for the parameters of Fig. 2. In this figure we observe a very large off-resonant peak which has a density-dependent position arising from the local-field effects. This large off-resonant peak is a characteristic of the enhanced electric susceptibility, which overshadows the contributions of the other susceptibilities when seen in this broad frequency scan of the refractive index. At the densities of interest, the magnetic susceptibility and chirality coefficients are amplified but have negligible frequency shifts since the quantity κ is dominated by the electric polarizability. The inset in Fig. 3 shows a zoomed in view of the refractive index at the original Raman and magnetic resonance frequencies. The enhancement of the chirality terms in Eq. (2) within this region causes the refractive index of the medium to sharply decrease, becoming negative, and this is accompanied by a flattening of the absorption approaching 0. For these parameters the refractive index reaches $n = -1$ with $F_M > 20$. It should be noted that in our technique it is necessary to have very low absorption in the electric susceptibility such that the local-field effects can optimally enhance the negative refraction of the medium.

To show the critical dependence on atomic density, Fig. 4 shows the refractive index for $N = 2 \times 10^{16}$ cm^{-3} and $N = 1 \times 10^{17}$ cm^{-3} with parameters otherwise identical to those of Fig. 3. For $N = 1 \times 10^{17}$ cm^{-3}, we obtain an index of refraction of $n = -2.77$ with low absorption. For $n = -1$ the $F_M \approx 40$.

Figure 5 shows the F_M achieved at the point Re$(n) = -1$ and the maximum F_M of the medium as the atomic density is varied with parameters otherwise identical to those in Figs. 2–4. For these parameters, the threshold density for a negative refractive index is $N = 6 \times 10^{15}$ cm^{-3}.

As mentioned above, for Figs. 2–5, the wavelengths for the electric-dipole ($|g\rangle \rightarrow |a\rangle, |b\rangle$) and magnetic-dipole ($|g\rangle \rightarrow |m\rangle$) transitions are assumed to be different by $\Delta\lambda = 0.1$ nm. This wavelength separation can be larger at the expense of an increase in the required control laser intensities. Figure 6 demonstrates this result. Here we plot the control laser intensity that is required to obtain results comparable to those of Figs. 2–5 as the wavelength separation between the transitions, $\Delta\lambda$, is varied. The transition wavelengths may be different by as much as $\Delta\lambda = 10$ nm and the scheme will still work with intensities that can be achieved with continuous-wave (cw) lasers (10 W laser beam focused down to about 1 μm). This increases the flexibility on the energy-level structure and, as we discuss below, may allow experimental implementation in a real atomic system.

We next discuss the sensitivity of our technique to various system parameters. As mentioned before, in our technique, it is critical to have vanishing absorption by appropriately
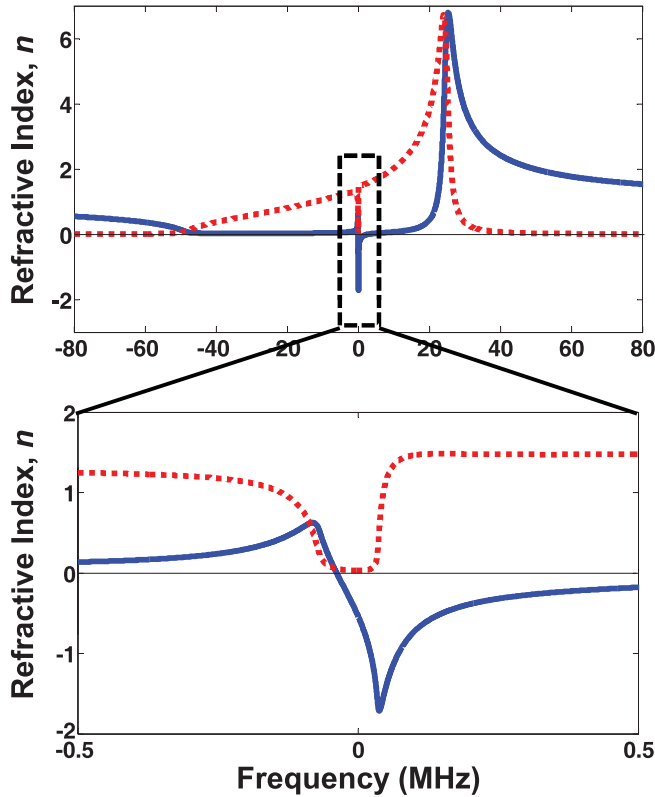
FIG. 5. (Color online) The figure of merit, $F_M = -\text{Re}(n)/|\text{Im}(n)|$, characterizes the performance of a negative index material. The solid blue line plots the F_M at the frequency position where $\text{Re}(n) = -1$ as the density of atoms is varied. The dashed red line plots the F_M at the frequency position where the F_M is maximized. The maximum F_M increases with increasing atomic density; however, at higher densities the maximum F_M occurs at frequencies where $\text{Re}(n) < -1$.

parameters identical to those of Fig. 3 ($N = 5 \times 10^{16}$ cm^{-3}). For the dashed lines, the intensity of the first control laser is decreased by 1%, whereas for the dotted lines it is decreased to 2% of the optimized value ($I_{c1} = 0.27$ MW/cm^2). We still observe $n \approx -1$ with a reasonably good F_M. Similarly, to address frequency jitter sensitivity, the solid lines in Fig. 8 show the real and imaginary parts of the refractive index for parameters identical to those in Fig. 3. For the the dashed lines, the frequency of the first control laser is shifted off resonance by 0.25 MHz, whereas for the dotted lines it is shifted by -0.25 MHz. We observe qualitatively similar behavior of negative refraction with reduced absorption.

V. NUMERICAL SIMULATIONS

In this section, we present exact numerical simulations to verify the predictions of the analytical results. For this purpose, we use the density-matrix formalism and numerically solve the

FIG. 3. (Color online) The real (solid blue) and imaginary (dotted red) parts of the index of refraction for an atomic density of $N = 5 \times 10^{16}$ cm^{-3}. The top plot shows a wide frequency scan of the resonant behavior and shows that at far-off resonance the medium returns to $n = 1$. The bottom plot shows the detailed features that occur at the Raman and magnetic resonances. The index of refraction becomes negative and reaches a value of $n = -1$ with a figure of merit $F_M > 20$.

interfering the two Raman transitions. We have varied parameters of the first control laser, which takes part in the gain Raman transition, to simulate fluctuations that would lead to imperfect interference of the Raman resonances. The solid lines in Fig. 7 show the real and imaginary parts of the refractive index for
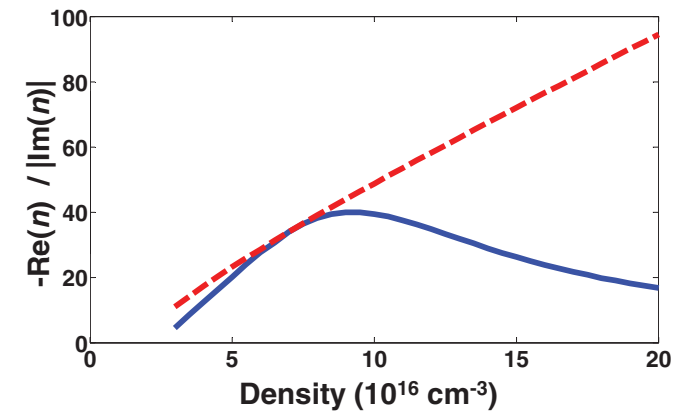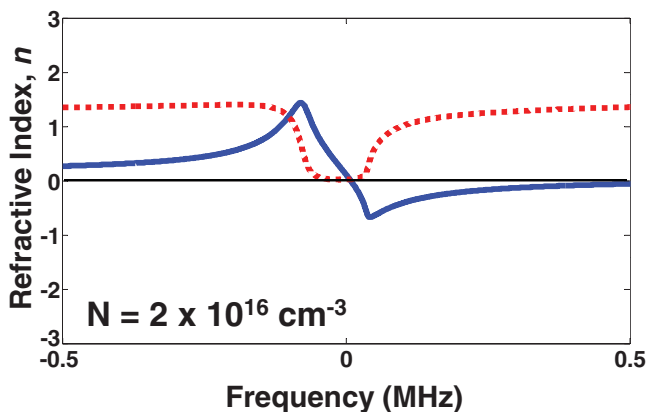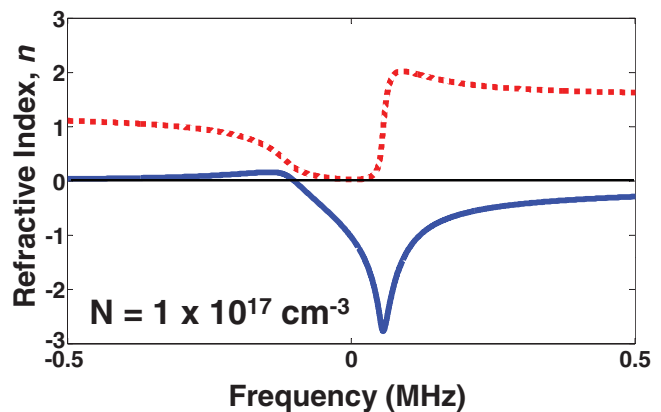

FIG. 4. (Color online) The real (solid blue) and imaginary (dotted red) parts of the index of refraction for an atomic density of $N = 2 \times 10^{16}$ cm^{-3} (left) and $N = 1 \times 10^{17}$ cm^{-3} (right). The other parameters are identical to those used in Fig. 3. For $N = 1 \times 10^{17}$ cm^{-3}, we obtain an index of refraction of $n = -1$ with a $F_M \approx 40$.
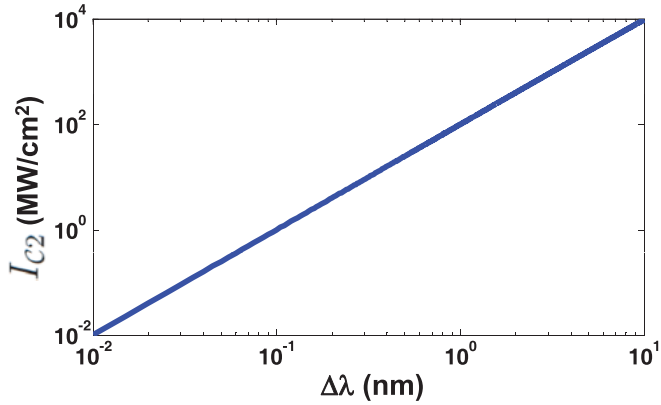
FIG. 6. (Color online) The control laser intensity, I_{C2}, required to obtain results comparable to those in Figs. 2–5 as a function of the wavelength separation between the transitions, $\Delta\lambda$. The control laser intensity, I_{C1}, follows a similar behavior (not shown).

evolution of the density-matrix elements, $\rho_{ij} \equiv c_i c_j^*$, for the full six-level system. The equations that describe the evolution of the 6×6 density matrix are shown in the Appendix. For a given set of system parameters, we numerically integrate these equations with the initial condition that the atoms start in the ground state, $\rho_{gg} = 1$, and the lasers fields are off and gradually turned on to full power in ≈ 400 ns. We use fourth-order Runge-Kutta as our numerical integration algorithm with a typical time grid spacing of ≈ 1 ps.

For the intensity values used in Figs. 2–5, using Eq. (13), the ac stark shifts calculated in our analytical formalism are on the order of 1 GHz, which is significantly higher than the linewidth of the resonances. Since the magnetic and two Raman resonances each experience a different ac Stark shift, we include adjustments to the tunings of the control lasers to ensure that all three resonances are aligned at the same frequency position. Initially we applied these analytical shift offsets in our numerical simulations, but we observed that frequency positions of the resonances could be misaligned by as much as 30 MHz. This is because of the breakdown of the perturbative approximation and therefore the analytical estimates of the Stark shifts are underestimated. To compensate

for this effect, we empirically applied additional shifts to the control laser frequencies such that all the resonances were aligned at the same frequency.

Figure 9 shows the numerically calculated coherences, ρ_{g1}, ρ_{g2}, and ρ_{gm}, for the parameters of Figs 2–5. For comparison, the coherences calculated through the analytical steady-state solutions of Eq. (10) are also plotted. As expected, the system quickly reaches steady state on time scales on the order of $1/\gamma_1 \approx 100$ ns. Once the system reaches steady-state, there is reasonable agreement between the numerical calculations and the analytical solutions. The discrepancy between the numerical and analytical solutions is due to effects that are related to the high intensity of the lasers, such as depopulation of the ground state and the breakdown of the perturbative approximation. We have checked that in the case of low-intensity laser fields there is very close agreement between the numerically and analytically calculated coherences. However these lower-intensity values are not sufficient to attain negative refraction.

Using the equations of the density matrix we numerically integrated the coherences as a function of time for a given frequency position until they reached a steady-state value. We then repeated this integration procedure for each frequency value in an array of equally spaced points to see the frequency dependence of the coherences as the probe beam is scanned across the resonance. The agreement between the numerical and analytical solutions can also be seen in Fig. 10, which plots the numerically solved values of the coherences and the analytical solutions as the probe frequency is scanned across the resonance.

There remained a discrepancy between the resulting coherences of our numerical simulation and our analytical results with the same parameters seen in Figs. 2–5. The strengths of the two Raman resonances were not properly balanced so as to lead to vanishing absorption. As mentioned earlier in Sec. IV, the local-field effects that result in negative refraction with minimal absorption are correlated with the vanishing absorption of the Raman resonances. To resolve this, we adjusted the strength of the gain Raman resonance from $I_{C1} = 0.27$ to 0.485 MW/cm^2 in our numerical simulations. Using this adjusted intensity, we were able to numerically calculate
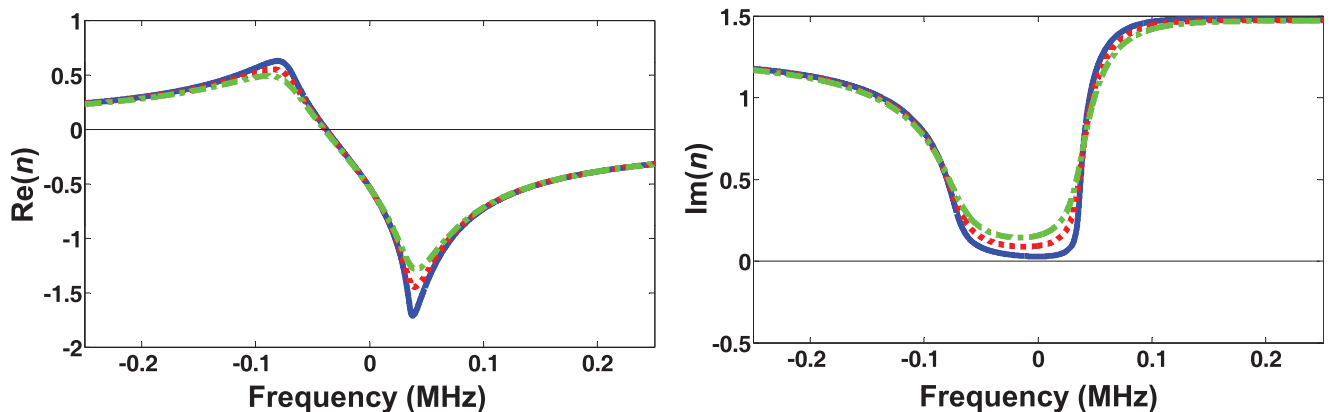

FIG. 7. (Color online) The real (left) and imaginary (right) parts of the index of refraction where the intensity of laser field $\mathcal{E}_{C1}$ is at 100% (solid blue line), 99% (red dotted line), and 98% (green dash-dotted line) of the optimized value of $I_{C1} = 0.27$ MW/cm^2 used in Figs. 2–4. The laser field $\mathcal{E}_{C1}$ interacts in the gain Raman resonance, which leads to reduced absorption.
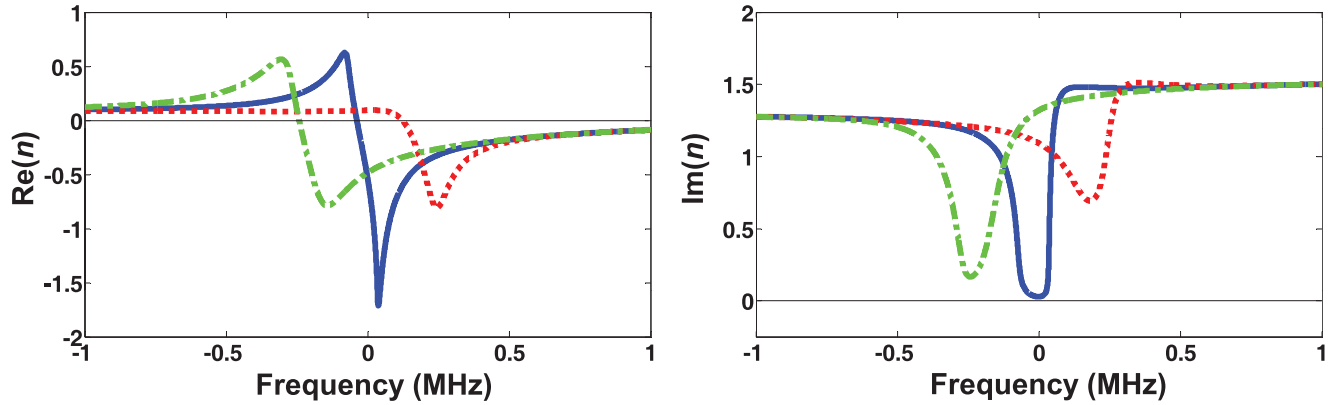
FIG. 8. (Color online) The real (left) and imaginary (right) parts of the index of refraction where the frequency of laser field $\mathcal{E}_{C1}$ is tuned on resonance (solid blue line) and off resonance by 0.25 MHz (red dotted line) and by -0.25 MHz (green dash-dotted line). As expected when the laser field is tuned off resonance the performance of the system as a negative index material decreases, but the features of negative refraction and reduced absorption remain qualitatively unchanged.

a refractive index that closely resembled our analytical results as seen in Fig. 11.

To gain insight into the discrepancies between the numerical and analytical results we considered the breakdown of the perturbative approximation in our analytical approach. Figure 12 shows the evolution of the population of the ground state, ρ_{gg}. Although the system initially starts in the ground state ($\rho_{gg} = 1$), the population of this state drops to $\rho_{gg} = 0.814$ as the laser fields are applied. The system, therefore, remains reasonably within the perturbative approximation since only about 18.6% of the population is moved from the ground state.

VI. EXPERIMENTAL IMPLEMENTATION IN RARE-EARTH METALS

In this section, we discuss possible experimental implementations of our technique in two rare-earth atomic species: erbium (Er) and dysprosium (Dy). By using Cowan's atomic structure code [66], we have found suitable transitions from the ground level in both of these atomic species. Further research may identify different atomic species and transitions that are better suited to our technique. However, we feel the two schemes in Er and Dy serve as a good starting point and also demonstrate the flexibility of our scheme. Figure 13 details the transitions in Er where we consider the $4f^{12}(^3H_6)6s^2\ ^3H_6(J=6) \rightarrow 4f^{12}(^1I_6)6s^2\ ^1I_6(J'=6)$ magnetic-dipole transition and the $4f^{12}(^3H_6)6s^2\ ^3H_6(J=6) \rightarrow 4f^{12}(^1G_4)6s6p(^1P_1^o)\ ^1H_5^o(J'=5)$ electric-dipole transition. The wavelengths of these two transitions are in the ultraviolet, and they differ by only 2.2 nm (335.3 nm for the magnetic-dipole transition and 337.5 nm for the electric-dipole transition). The ^{167}Er isotope has a nuclear spin of $I = 7/2$ and occurs with a natural abundance of 23%. The resulting hyperfine levels [67,68] can be used to induce Raman transitions with the probe and the control lasers. By using Cowan's code we have calculated the magnetic-dipole reduced matrix element to be $\langle J||\hat{\mu}||J'\rangle = 0.1\mu_B$ (μ_B, Bohr magneton) and the electric-dipole reduced matrix element to be $\langle J||\hat{d}||J'\rangle = 0.2ea_0$ (e, electron charge; a_0, Bohr radius), both of which are reasonably strong.

For dysprosium, we consider the ^{161}Dy isotope (natural abundance of 19%, nuclear spin of $I = 5/2$) with a level structure similar to that of Fig. 13. We have identified the $4f^{10}(^5I_8)6s^2\ ^5I_8(J=8) \rightarrow 4f^{10}(^3K_7)6s^2\ ^3K_7(J'=7)$ and the $4f^{10}(^5I_8)6s^2\ ^5I_8(J=8) \rightarrow 4f^9(^2M_{17/2}^o)5d_{3/2}6s^2\ ^5K_7^o(J'=7)$ magnetic and electric-dipole transitions as suitable candidates for our technique. The wavelengths of these two transitions are 484 nm for the magnetic-dipole transition and 484.8 nm for the electric-dipole transition. The calculated reduced matrix elements for the two transitions are $\langle J||\hat{\mu}||J'\rangle = 0.06\mu_B$ and $\langle J||\hat{d}||J'\rangle = 0.19ea_0$, respectively. Although these matrix elements are slightly weaker than those of erbium, ^{161}Dy has the key advantage that the electric and magnetic transition wavelengths are closer. The hyperfine splitting of the ground level for ^{161}Dy is about 1 GHz [69].

Obtaining negative refraction with the parameters of Figs. 2–5 (densities exceeding 10^{16} cm^{-3} with optical transition linewidths at the MHz level) will undoubtedly be a very challenging experiment, and there are many open questions. For experimental implementation of our approach with rare-earth atoms, three types of atomic systems may be utilized: (i) atomic beams moving orthogonal to the laser propagation direction to allow for Doppler-free interaction [70], (ii) laser-cooled and trapped high-density ultracold atomic clouds [71–74], or (iii) magnetically trapped atom clouds cooled through buffer gas cooling [75]. A detailed theoretical modeling to investigate negative refraction with these three different atomic systems will be among our future investigations. The modeling will need to go beyond what we have discussed in the previous section and will include effects such as the collisional broadening of the magnetic transition, dipole-dipole interactions, and various inelastic and elastic collision processes. The collisional broadening and dipole-dipole interactions will determine the magnetic transition and Raman linewidths and will have a direct effect on the magnitude of the refractive index that can be achieved. We note that, since the laser beams are far-detuned from the electric-dipole transition, our scheme is less sensitive to the broadening of the excited electronic states $|a\rangle$ and $|b\rangle$. The inelastic and elastic collision processes will determine the
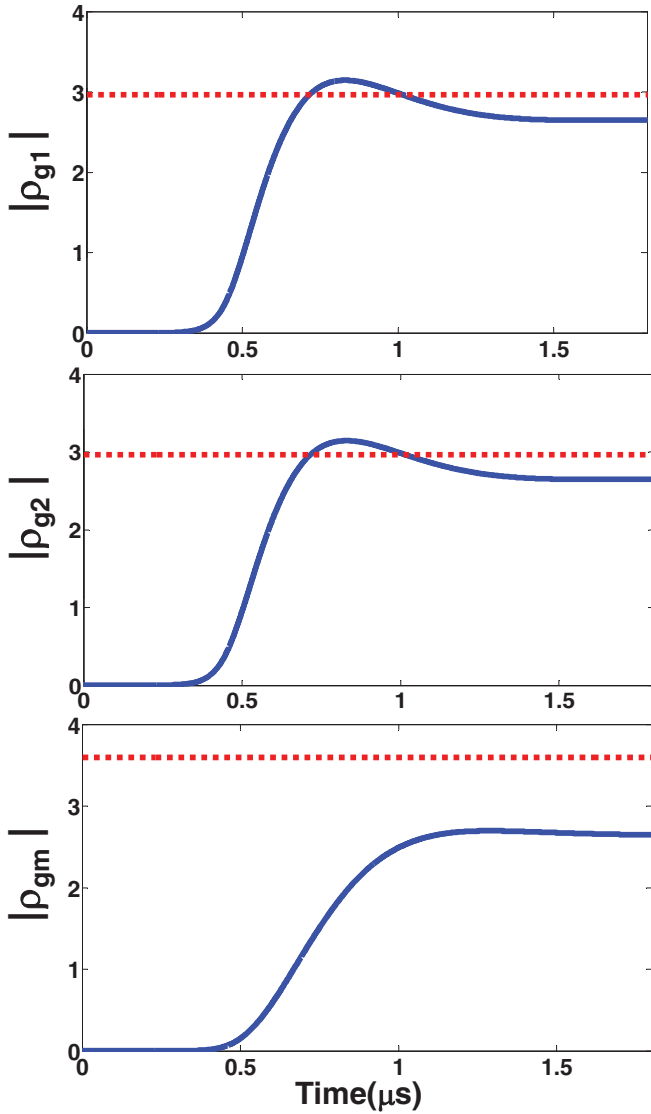
FIG. 9. (Color online) The numerically solved values (solid blue lines) of the coherences ρ_{g1}, ρ_{g2}, and ρ_{gm} (in arbitrary units) as they evolve in time with the intensity of the laser beams gradually applied. The coherences approach a steady-state value in a little under 2 μs. The analytical formalism steady-state solutions (red dotted lines) of the coherences are shown for comparison. The frequency of the probe beam is taken to be on the Raman and magnetic resonances.
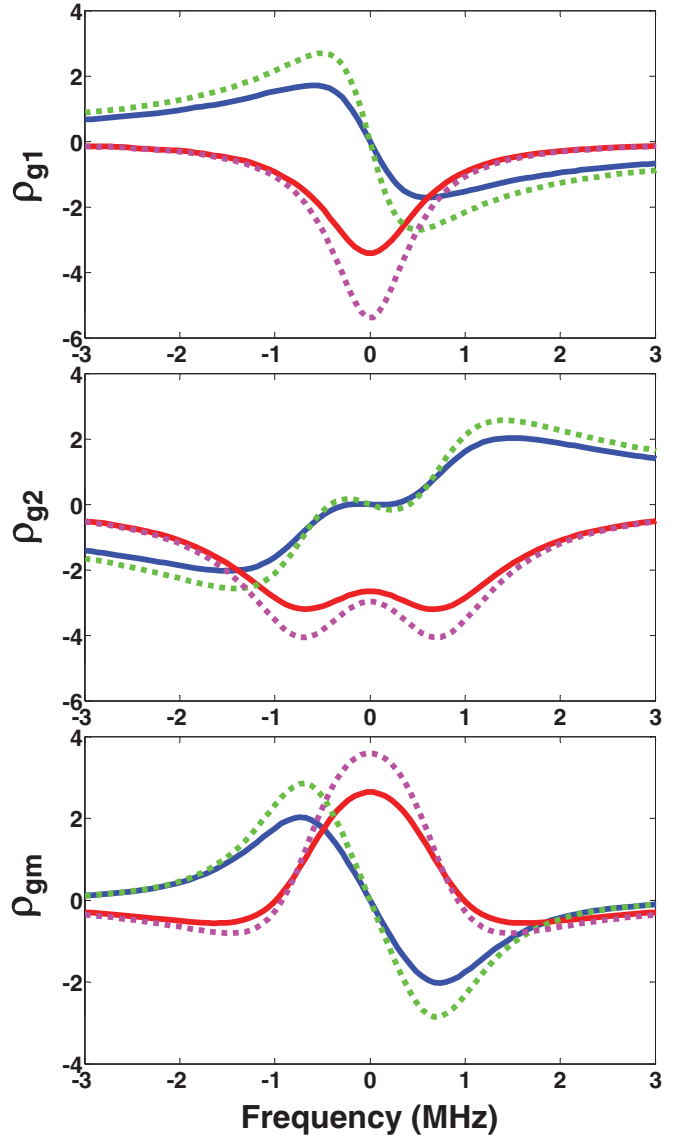
FIG. 10. (Color online) The real (solid blue line) and imaginary (solid red line) parts of the numerically solved steady-state values of the coherences ρ_{g1}, ρ_{g2}, and ρ_{gm} (in arbitrary units) as they are scanned across resonance. These are compared to the real (dotted green line) and imaginary (dotted magenta line) parts of the coherences calculated using the analytical steady-state solutions with the same parameters.

largest achievable densities in the trap. The cross sections for most of these processes are not known, but some progress has been made experimentally [76]. Furthermore, it may be possible to calculate some of these cross sections using *ab initio* methods [66].

Below, we briefly discuss the advantages and disadvantages of each of the experimental approaches. We also detail the preliminary experimental steps that can be pursued before negative refraction is achieved.

A. Atomic beams

It is well-known that atomic beams with a small transverse velocity spread can be produced using relatively simple experimental methods. Typical rare-earth atomic beam ex-

periments start with vapors inside resistively heated ovens at temperatures exceeding 1000 °C. Several spatial apertures are then used to produce a well-collimated beam. For atomic beams, the Doppler interaction can be greatly reduced using geometries where the beam direction is orthogonal to the laser propagation direction. The spectroscopy of optical lines at the MHz level can be performed using these techniques [70]. The key challenges of using atomic beams are the following. (i) There is a trade-off between the achieved density and the collimation and transverse temperature of the beam. It remains to be seen whether sufficiently high densities with sufficiently good beam quality can be achieved using this approach. (ii) The interaction time of the atoms with the laser beams is limited by the transit time, which produces an undesirable additional
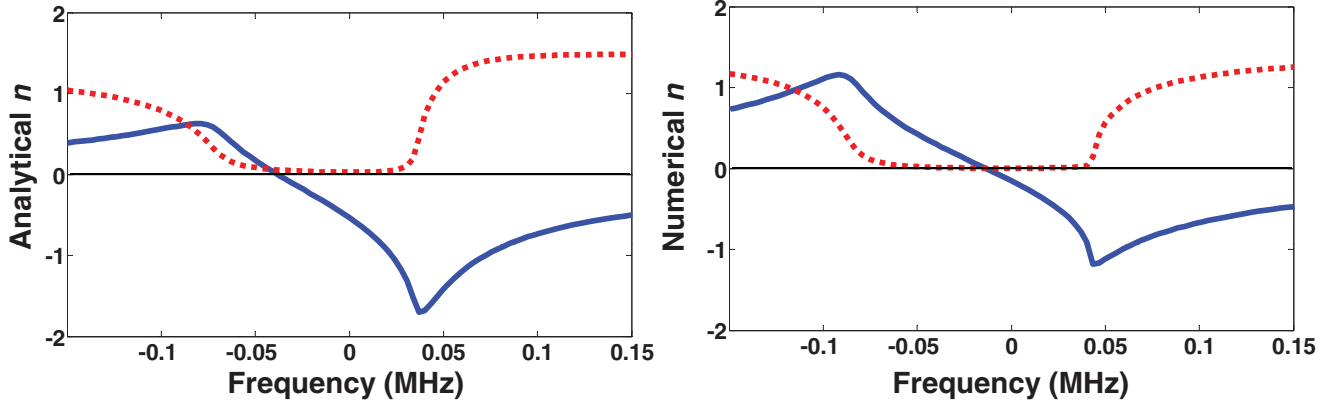
FIG. 11. (Color online) The real (solid blue line) and imaginary (dotted red line) parts of the index of refraction as calculated using our analytical formalism (left) and our numerically solved model (right) for a density of $N = 5 \times 10^{16}$ cm^{-3}. All of the parameters are the same, except the intensity of laser field $\mathcal{E}_{C1}$ was adjusted to $I_{C1} = 0.485$ MW/cm^2 in the numerical model from the value used in previous figures of $I_{C1} = 0.27$ MW/cm^2, which was used in the analytical result.

broadening mechanism. We plan to carefully evaluate these issues and to explore the feasibility of these systems for achieving negative refraction.

B. Cooling and trapping

Both Er and Dy have been laser cooled and trapped recently with trapped atom numbers as high as half a billion and atomic temperatures at the μK level [71–74]. Although the structure of these atoms is highly complex, laser cooling is possible because of the large magnetic moment of these atoms. The metastable states are trapped in a quadrupole magnetic field and laser cooling is achieved without any repumping lasers, the so-called "repumperless" MOT (magneto-optical trap).

It is well-known that MOTs are not suitable for achieving very high atomic densities due to effects such as radiation trapping. To obtain high-density atomic clouds, one approach is to construct an optical dipole trap. Such dipole traps can be formed by focusing an intense very-far-detuned laser beam overlapping with the MOT cloud. Recently, ultracold atomic densities approaching 10^{15} cm^{-3} have been demonstrated in atomic ytterbium (Yb) [77]. By using evaporative cooling in

the optical trap, such clouds can be cooled to quantum degeneracy and the formation of a Yb Bose-Einstein condensate (BEC) has been recently achieved [78–81]. These are very exciting developments, and we feel that high-density clouds in optical dipole traps show considerable promise for the study of negative refraction. In addition to studies of negative refraction, such traps will likely have significant implications for other research areas including precision spectroscopy and dipolar physics [74].

An alternative approach to laser cooling is buffer gas cooling and magnetic trapping [75]. Although buffer gas cooling only achieves mK level temperatures, the trapped atom numbers are significantly higher. Using this approach, Doyle and colleagues have demonstrated trapping of about 10^{12} atoms in many of the rare-earth species, including Er and Dy [75]. Due to the large initial trapped atom number, buffer
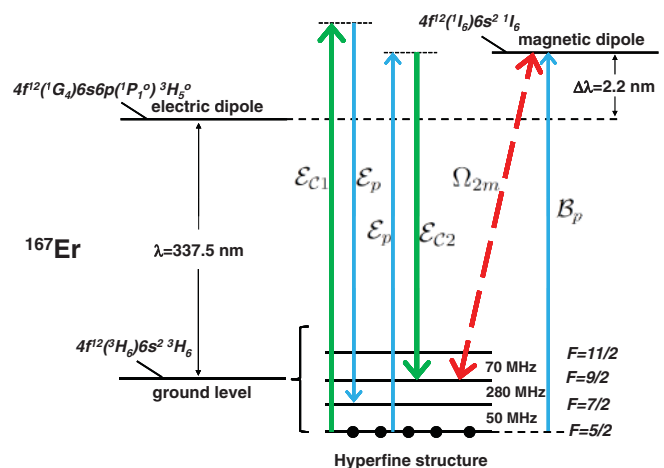
FIG. 13. (Color online) The proposed experimental scheme in atomic ^{167}Er. The hyperfine structure of the ground level is used to induce Raman transitions with the probe beam and the control lasers. For simplicity, the hyperfine structure of the excited levels is not shown. A similar level scheme can also be found for atomic ^{161}Dy (see text for details). The central wavelength for ^{161}Dy is 484.8 nm and the difference of the two transition wavelengths is $\Delta\lambda = 0.8$ nm.
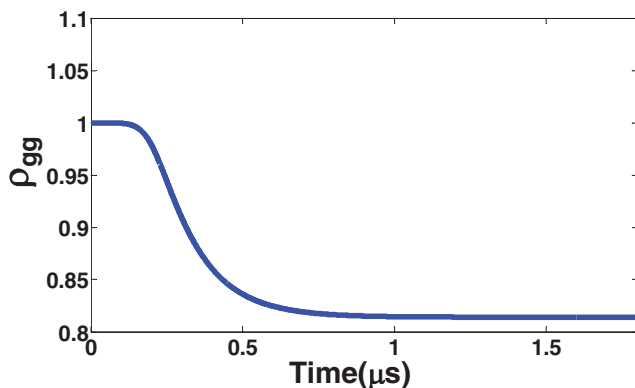

FIG. 12. (Color online) The ground-state population of the system in our numerical simulation initially starts at 100% and decreases in time as the laser fields are gradually turned on, eventually reaching a steady-state value of 81.4%.

gas cooling and magnetic trapping may serve as an excellent starting point for producing high-density clouds. By using evaporative cooling in the magnetic trap, or by transferring atoms to a dipole trap and then performing evaporative cooling, it will likely be possible to achieve densities exceeding 10^{15} cm^{-3} using this approach.

C. Spectroscopy of electric-dipole and magnetic-dipole transitions

For a given atomic system, a first goal would be to perform spectroscopic measurements of the predicted magnetic-dipole and electric-dipole transitions. These measurements are needed to verify the hyperfine structure and to confirm linewidths and transition matrix elements. One also needs to demonstrate the ability to perform optical pumping to a specific ground hyperfine level. Such hyperfine-level initialization is critical to performing Raman transitions within the ground-level manifold. To understand the density limitations, the electric-dipole and magnetic-dipole transition line shapes at different densities can be measured. This will allow the density broadening and dipole-dipole interaction coefficients to be deduced.

D. Stimulated Raman transitions

As mentioned before, Raman transitions between the hyperfine levels in the ground-level manifold can be utilized. The hyperfine-level spacing in rare-earth atoms is typically in the 100 MHz to 1 GHz range. This allows the probe beam, $\mathcal{E}_p$, and the two control lasers, $\mathcal{E}_{\mathcal{C}1}$ and $\mathcal{E}_{\mathcal{C}2}$, to be obtained from the same laser system by using high-frequency acousto-optic modulators. Both the absorption (or gain) and the phase shift due to the Raman transitions (the real and imaginary parts of the Raman line shapes) can be measured with techniques similar to the ones used in Ref. [57].

E. Magnetoelectric coupling (chirality)

The next goal would be to demonstrate magnetoelectric (chiral) response. Chiral response may be achieved at low densities and a basic form of chirality has already been demonstrated in Rb vapor [82]. As discussed in previous sections, the magnetoelectric coupling results in large contributions to the refractive index. One approach would, therefore, be to study the real and imaginary parts of the refractive index (absorption and phase shift) for the probe wave, as the strength or the phase of the cross-coupling rate, Ω_{2m}, is varied. With $\Omega_{2m} = 0$ (no cross-coupling), the system reduces to three resonances (two electric-dipole Raman resonances and a magnetic resonance). As a starting point, these three resonances can be studied independently. As Ω_{2m} increases, the interference and the cross-coupling of these resonances will be observable.

F. Rare-earth-doped crystals

We conclude this section by noting that crystals that are doped with rare-earth atoms are an alternative route for the study of negative refraction with atomic systems. These systems are somewhat different than the atomic gases that we have focused on so far and pose different types of challenges. It is well known that at cryogenic temperatures the homogeneous linewidths can be at the MHz level and many quantum coherence effects such as EIT have been observed in these crystals [83–88]. The key difficulty with these systems is the large inhomogeneous broadening which is many orders of magnitude larger than the homogeneous linewidth. Typical EIT experiments use spectral hole burning techniques and frequency-selective optical pumping to overcome this difficulty. However, such techniques result in a decrease in the effective atomic density and therefore will have a detrimental effect on negative refraction experiments. We plan to put significant theoretical effort into investigating these issues and exploring the feasibility of these systems for achieving negative refraction.

VII. CONCLUSIONS

To summarize, we have outlined a Raman-based approach for achieving a negative index of refraction with low absorption in the optical region of the spectrum. Differing from the metamaterial approach, our technique utilizes atomic systems that are driven with lasers in their internal states. The key advantage of our approach is that our technique does not require the simultaneous presence of an electric-dipole transition and a magnetic-dipole transition near the same wavelength. This gives large flexibility in the requirements for the energy-level structure, and we have identified Er and Dy as possible candidates for experimental implementation.

There are many open questions that yet need to be addressed. One future direction would be to perform detailed theoretical modeling to identify the most suitable atomic species and experimental system for observing negative refraction. As discussed above, each experimental approach has various advantages and drawbacks, and a careful evaluation of the achievable atomic densities and the linewidths is needed. If achieved, negative refraction in atomic systems may have significant implications for a number of research areas. As mentioned above, one key practical application is in optical imaging science. As the frontiers of science and engineering approach the nanoscale, it becomes ever more important to devise optical imaging techniques with nanometer resolution. In recent years, overcoming the diffraction barrier has been the subject of intense theoretical and experimental research [89–96]. Perfect lenses constructed from negative index materials may provide a unique approach for resolving nanoscale objects and may therefore have far-reaching practical implications. These devices may also be used to reduce the smallest feature size of a lithographic mask. This is particularly important since lithographic resolution currently determines the size and the processing power of every semiconductor integrated circuit.

APPENDIX: DENSITY MATRIX EQUATIONS

In this section, we present the equations for the density-matrix elements that were used for the numerical simulations of Sec. V. We define the Rabi coupling rate between respective levels $|i\rangle$ and $|j\rangle$ to be $\Omega_{ij} \equiv d_{ij}\mathcal{E}_k/\hbar$ for electric-dipole transitions and $\Omega_{ij} \equiv \mu_{ij}\mathcal{B}_k/\hbar$ for magnetic-dipole transitions,

where $\mathcal{E}_k$ and $\mathcal{B}_k$ are the relevant field terms coupling the states as seen in Fig. 1. We also define the one-photon detunings $\delta\omega_a \equiv \omega_a - \omega_g - \omega_{\mathcal{C}1}$ and $\delta\omega_b \equiv \omega_b - \omega_g - \omega_p$. Using the evolution equations for the probability amplitudes of Eq. (4), the density-matrix elements $\rho_{ij} \equiv c_i c_j^*$ evolve according to

$$\dot{\rho}_{gg} = -\gamma_g \rho_{gg} + \frac{\Gamma_a}{3}\rho_{aa} + \frac{\Gamma_b}{3}\rho_{bb} + \gamma_1 \rho_{11} + \gamma_2 \rho_{22} + \gamma_m \rho_{mm} + \frac{i}{2}(\rho_{gm}^* \Omega_{gm} + \rho_{ga}^* \Omega_{ga} + \rho_{gb}^* \Omega_{gb} - \text{H.c.}),$$

$$\dot{\rho}_{g1} = \frac{i2\delta\omega_1 - (\gamma_1 + \gamma_g)}{2}\rho_{g1} + \frac{i}{2}(-\rho_{gm}\Omega_{1m}^* - \rho_{ga}\Omega_{1a}^* + \rho_{1m}^* \Omega_{gm} + \rho_{1a}^* \Omega_{ga} + \rho_{1b}^* \Omega_{gb}),$$

$$\dot{\rho}_{g2} = \frac{i2\delta\omega_2 - (\gamma_2 + \gamma_g)}{2}\rho_{g2} + \frac{i}{2}(-\rho_{gm}\Omega_{2m}^* - \rho_{gb}\Omega_{2b}^* + \rho_{2m}^* \Omega_{gm} + \rho_{2a}^* \Omega_{ga} + \rho_{2b}^* \Omega_{gb}),$$

$$\dot{\rho}_{gm} = \frac{i2\delta\omega_\mathcal{B} - (\gamma_m + \gamma_g)}{2}\rho_{gm} + \frac{i}{2}[-\rho_{g1}\Omega_{1m} - \rho_{g2}\Omega_{2m} + (\rho_{mm} - \rho_{gg})\Omega_{gm} + \rho_{ma}^* \Omega_{ga} + \rho_{mb}^* \Omega_{gb}],$$

$$\dot{\rho}_{ga} = \frac{i2\delta\omega_a - (\Gamma_a + \gamma_g)}{2}\rho_{ga} + \frac{i}{2}[-\rho_{g1}\Omega_{1a} + \rho_{ma}\Omega_{gm} + (\rho_{aa} - \rho_{gg})\Omega_{ga} + \rho_{ab}^* \Omega_{gb}],$$

$$\dot{\rho}_{gb} = \frac{i2\delta\omega_b - (\Gamma_b + \gamma_g)}{2}\rho_{gb} + \frac{i}{2}[-\rho_{g2}\Omega_{2b} + \rho_{mb}\Omega_{gm} + (\rho_{bb} - \rho_{gg})\Omega_{gb} + \rho_{ab}\Omega_{ga}],$$

$$\dot{\rho}_{11} = -\gamma_1 \rho_{11} + \frac{\Gamma_a}{3}\rho_{aa} + \frac{\Gamma_b}{3}\rho_{bb} + \frac{i}{2}(\rho_{1m}^* \Omega_{1m} + \rho_{1a}^* \Omega_{1a} - \text{H.c.}),$$

$$\dot{\rho}_{12} = \frac{i2(\delta\omega_2 - \delta\omega_1) - (\gamma_1 + \gamma_2)}{2}\rho_{12} - \frac{i}{2}(-\rho_{2m}^* \Omega_{1m} - \rho_{2a}^* \Omega_{1a} + \rho_{1m}\Omega_{2m}^* + \rho_{1b}\Omega_{2b}^*),$$

$$\dot{\rho}_{1m} = \frac{i2(\delta\omega_\mathcal{B} - \delta\omega_1) - (\gamma_1 + \gamma_m)}{2}\rho_{1m} + \frac{i}{2}[(\rho_{mm} - \rho_{11})\Omega_{1m} + \rho_{ma}^* \Omega_{1a} - \rho_{12}\Omega_{2m} - \rho_{g1}^* \Omega_{gm}],$$

$$\dot{\rho}_{1a} = \frac{i2(\delta\omega_a - \delta\omega_1) - (\gamma_1 + \Gamma_a)}{2}\rho_{1a} + \frac{i}{2}[(\rho_{aa} - \rho_{11})\Omega_{1a} + \rho_{ma}\Omega_{1m} - \rho_{g1}^* \Omega_{ga}],$$

$$\dot{\rho}_{1b} = \frac{i2(\delta\omega_b - \delta\omega_1) - (\gamma_1 + \Gamma_b)}{2}\rho_{1b} + \frac{i}{2}(\rho_{mb}\Omega_{1m} + \rho_{ab}\Omega_{1a} - \rho_{12}\Omega_{2b} - \rho_{g1}^* \Omega_{gb}),$$

$$\dot{\rho}_{22} = -\gamma_2 \rho_{22} + \frac{\Gamma_a}{3}\rho_{aa} + \frac{\Gamma_b}{3}\rho_{bb} + \frac{i}{2}(\rho_{2m}^* \Omega_{2m} + \rho_{2b}^* \Omega_{2b} - \text{H.c.}),$$

$$\dot{\rho}_{2m} = \frac{i2(\delta\omega_\mathcal{B} - \delta\omega_2) - (\gamma_2 + \gamma_m)}{2}\rho_{2m} + \frac{i}{2}[(\rho_{mm} - \rho_{22})\Omega_{2m} - \rho_{12}^* \Omega_{1m} + \rho_{mb}^* \Omega_{2b} - \rho_{g2}^* \Omega_{gm}],$$

$$\dot{\rho}_{2a} = \frac{i2(\delta\omega_a - \delta\omega_2) - (\gamma_2 + \Gamma_a)}{2}\rho_{2a} + \frac{i}{2}(-\rho_{12}^* \Omega_{1a} + \rho_{ma}\Omega_{2m} + \rho_{ab}^* \Omega_{2b} - \rho_{g2}^* \Omega_{ga}),$$

$$\dot{\rho}_{2b} = \frac{i2(\delta\omega_b - \delta\omega_2) - (\gamma_2 + \Gamma_b)}{2}\rho_{2b} + \frac{i}{2}[(\rho_{bb} - \rho_{22})\Omega_{2b} + \rho_{mb}\Omega_{2m} - \rho_{g2}^* \Omega_{gb}],$$

$$\dot{\rho}_{mm} = -\gamma_m \rho_{mm} + \frac{i}{2}(\rho_{1m}\Omega_{1m}^* + \rho_{2m}\Omega_{2m}^* + \rho_{gm}\Omega_{gm}^* - \text{H.c.}),$$

$$\dot{\rho}_{ma} = \frac{i2(\delta\omega_a - \delta\omega_\mathcal{B}) - (\gamma_m + \Gamma_a)}{2}\rho_{ma} - \frac{i}{2}(-\rho_{1a}\Omega_{1m}^* + \rho_{1m}^* \Omega_{1a} - \rho_{2a}\Omega_{2m}^* - \rho_{ga}\Omega_{gm}^* + \rho_{gm}^* \Omega_{ga}),$$

$$\dot{\rho}_{mb} = \frac{i2(\delta\omega_b - \delta\omega_\mathcal{B}) - (\gamma_m + \Gamma_b)}{2}\rho_{mb} - \frac{i}{2}(-\rho_{1b}\Omega_{1m}^* + \rho_{2m}^* \Omega_{2b} - \rho_{2b}\Omega_{2m}^* - \rho_{gb}\Omega_{gm}^* + \rho_{gm}^* \Omega_{gb}),$$

$$\dot{\rho}_{aa} = -\Gamma_a \rho_{aa} + \frac{i}{2}(\rho_{1a}\Omega_{1a}^* + \rho_{ga}\Omega_{ga}^* - \text{H.c.}),$$

$$\dot{\rho}_{ab} = \frac{i2(\delta\omega_b - \delta\omega_a) - (\Gamma_a + \Gamma_b)}{2}\rho_{ab} - \frac{i}{2}(-\rho_{1b}\Omega_{1a}^* + \rho_{2a}^* \Omega_{2b} - \rho_{gb}\Omega_{ga}^* + \rho_{ga}^* \Omega_{gb}),$$

$$\dot{\rho}_{bb} = -\Gamma_b \rho_{bb} + \frac{i}{2}(\rho_{2b}\Omega_{2b}^* + \rho_{gb}\Omega_{gb}^* - \text{H.c.}). \tag{A1}$$

The remaining elements of the 6×6 density matrix can be found using $\rho_{ij} = \rho_{ji}^*$.

[1] V. G. Veselago, Sov. Phys. Usp. **10**, 509 (1968).

[2] J. B. Pendry, Phys. Rev. Lett. **85**, 3966 (2000).

[3] D. R. Smith and N. Kroll, Phys. Rev. Lett. **85**, 2933 (2000).

[4] S. Foteinopoulou, E. N. Economou, and C. M. Soukoulis, Phys. Rev. Lett. **90**, 107402 (2003).

[5] R. A. Shelby, D. R. Smith, and S. Shultz, Science **292**, 77 (2001).

[6] A. A. Houck, J. B. Brock, and I. L. Chuang, Phys. Rev. Lett. **90**, 137401 (2003).

[7] P. V. Parimi, W. T. Lu, P. Vodo, J. Sokoloff, J. S. Derov, and S. Sridhar, Phys. Rev. Lett. **92**, 127401 (2004).

[8] E. Cubukcu, K. Aydin, E. Ozbay, S. Foteinopoulou, and C. M. Soukoulis, Nature (London) **423**, 604 (2003).

[9] E. Cubukcu, K. Aydin, E. Ozbay, S. Foteinopoulou, and C. M. Soukoulis, Phys. Rev. Lett. **91**, 207401 (2003).

[10] T. J. Yen, W. J. Padilla, N. Fang, D. C. Vier, D. R. Smith, J. B. Pendry, D. N. Basov, and X. Zhang, Science **303**, 1494 (2004).

[11] N. Fang, H. Lee, C. Sun, and X. Zhang, Science **308**, 534 (2005).

[12] V. M. Shalaev, W. Cai, U. K. Chettiar, H. Yuan, A. K. Sarychev, V. P. Drachev, and A. V. Kildishev, Opt. Lett. **30**, 3356 (2005).

[13] U. K. Chettiar, A. V. Kildishev, H. Yuan, W. Cai, S. Xiao, V. P. Drachev, and V. M. Shalaev, Opt. Lett. **32**, 1671 (2007).

[14] S. Xiao, U. K. Chettiar, A. V. Kildishev, V. P. Drachev, and V. M. Shalaev, Opt. Lett. **34**, 3478 (2009).

[15] S. Zhang, W. Fan, N. C. Panoiu, K. J. Malloy, R. M. Osgood, and S. R. J. Brueck, Phys. Rev. Lett. **95**, 137404 (2005).

[16] G. Dolling, C. Enrich, M. Wegener, C. M. Soukoulis, and S. Linden, Opt. Lett. **31**, 1800 (2006).

[17] G. Dolling, M. Wegener, C. M. Soukoulis, and S. Linden, Opt. Lett. **32**, 53 (2007).

[18] G. Dolling, M. Wegener, C. M. Soukoulis, and S. Linden, Opt. Lett. **32**, 53 (2007).

[19] M. S. Rill, C. Plet, Michael Thiel, I. Staude, G. Freymann, S. Linden, and M. Wegener, Nat. Mater.**7**, 543 (2008).

[20] H. J. Lezec, J. A. Dionne, and H. A. Atwater, Science **316**, 430 (2007).

[21] D. Schurig, J. J. Mock, B. J. Justice, S. A. Cummer, J. B. Pendry, A. F. Starr, and D. R. Smith, Science **314**, 977 (2006).

[22] J. Valentine, J. Li, T. Zentgraf, G. Bartal, and X. Zhang, Nat. Mater. **8**, 568 (2009).

[23] D. E. Sikes and D. D. Yavuz, Phys. Rev. A **82**, 011806(R) (2010).

[24] M. O. Oktel and O. E. Mustecaplioglu, Phys. Rev. A **70**, 053806 (2004).

[25] Q. Thommen and P. Mandel, Phys. Rev. Lett. **96**, 053601 (2006).

[26] J. B. Pendry, Science **306**, 1353 (2004).

[27] C. Monzon and D. W. Forester, Phys. Rev. Lett. **95**, 123904 (2005).

[28] J. Kästel, M. Fleischhauer, S. F. Yelin, and R. L. Walsworth, Phys. Rev. Lett. **99**, 073602 (2007).

[29] J. Kästel, M. Fleischhauer, S. F. Yelin, and R. L. Walsworth, Phys. Rev. A **79**, 063818 (2009).

[30] M. O. Scully and M. S. Zubairy, *Quantum Optics* (Cambridge University Press, Cambridge, UK, 1997).

[31] S. E. Harris, Phys. Today **50**, 36 (1997).

[32] O. Kocharovskaya and P. Mandel, Phys. Rev. A **42**, 523 (1990).

[33] J. Gea-Banacloche, Y. Q. Li, S. Z. Jin, and M. Xiao, Phys. Rev. A **51**, 576 (1995).

[34] A. Kasapi, M. Jain, G. Y. Yin, and S. E. Harris, Phys. Rev. Lett. **74**, 2447 (1995).

[35] M. Xiao, Y. Q. Li, S. Z. Jin, and J. Gea-Banacloche, Phys. Rev. Lett. **74**, 666 (1995).

[36] L. V. Hau, S. E. Harris, Z. Dutton, and C. H. Behroozi, Nature (London) **397**, 594 (1999).

[37] M. M. Kash, V. A. Sautenkov, A. S. Zibrov, L. Hollberg, G. R. Welch, M. D. Lukin, Y. Rostovtsev, E. S. Fry, and M. O. Scully, Phys. Rev. Lett. **82**, 5229 (1999).

[38] G. M. Gehring, A. Schweinsberg, C. Barsi, N. Kostinski, and R. W. Boyd, Science **312**, 895 (2007).

[39] M. Fleischhauer and M. D. Lukin, Phys. Rev. Lett. **84**, 5094 (2000).

[40] D. F. Phillips, A. Fleischhauer, A. Mair, R. L. Walsworth, and M. D. Lukin, Phys. Rev. Lett. **86**, 783 (2001).

[41] C. Liu, Z. Dutton, C. H. Behroozi, and L. V. Hau, Nature (London) **409**, 6819 (2001).

[42] I. Novikova, A. V. Gorshkov, D. F. Phillips, A. S. Sorensen, M. D. Lukin, and R. L. Walsworth, Phys. Rev. Lett. **98**, 243602 (2007).

[43] N. B. Phillips, A. V. Gorshkov, and I. Novikova, Phys. Rev. A **78**, 023801 (2008).

[44] H. Schmidt and A. Imamoglu, Opt. Lett. **21**, 1936 (1996).

[45] A. Imamoglu, H. Schmidt, G. Woods, and M. Deutsch, Phys. Rev. Lett. **79**, 1467 (1997).

[46] S. E. Harris and Y. Yamamoto, Phys. Rev. Lett. **81**, 3611 (1998).

[47] S. E. Harris and L. V. Hau, Phys. Rev. Lett. **82**, 4611 (1999).

[48] M. D. Lukin and A. Imamoglu, Phys. Rev. Lett. **84**, 1419 (2000).

[49] H. Wang, D. Goorskey, and M. Xiao, Phys. Rev. Lett. **87**, 073601 (2001).

[50] M. Yan, E. G. Rickey, and Y. Zhu, Phys. Rev. A **64**, 041801 (2001).

[51] H. Kang and Y. Zhu, Phys. Rev. Lett. **91**, 093601 (2003).

[52] D. A. Braje, V. Balic, S. Goda, G. Y. Yin, and S. E. Harris, Phys. Rev. Lett. **93**, 183601 (2004).

[53] V. Balic, D. A. Braje, P. Kolchin, G. Y. Yin, and S. E. Harris, Phys. Rev. Lett. **94**, 183601 (2005).

[54] P. Kolchin, S. Du, C. Belthangady, G. Y. Yin, and S. E. Harris, Phys. Rev. Lett. **97**, 113602 (2006).

[55] D. D. Yavuz, Phys. Rev. Lett. **95**, 223601 (2005).

[56] P. Anisimov and O. Kocharovskaya, invited talk, 38th Winter Colloquium on Physics of Quantum Electronics, Snowbird, UT, 2008.

[57] N. A. Proite, B. E. Unks, J. T. Green, and D. D. Yavuz, Phys. Rev. Lett. **101**, 147401 (2008).

[58] D. D. Yavuz and N. A. Proite, Phys. Rev. A **78**, 053811 (2008).

[59] M. O. Scully, Phys. Rev. Lett. **67**, 1855 (1991).

[60] M. O. Scully and M. Fleischhauer, Phys. Rev. Lett. **69**, 1360 (1992).

[61] M. Fleischhauer, C. H. Keitel, M. O. Scully, C. Su, B. T. Ulrich, and S. Y. Zhu, Phys. Rev. A **46**, 1468 (1992).

[62] U. Rathe, M. Fleischhauer, S. Y. Zhu, T. W. Hansch, and M. O. Scully, Phys. Rev. A **47**, 4994 (1993).

[63] A. S. Zibrov, M. D. Lukin, L. Hollberg, D. E. Nikonov, M. O. Scully, H. G. Robinson, and V. L. Velichansky, Phys. Rev. Lett. **76**, 3935 (1996).

[64] D. M. Cook, *Theory of the Electromagnetic Field* (Prentice Hall, New York, 1975).

[65] J. Kästel, M. Fleischhauer, and G. Juzeliūnas, Phys. Rev. A **76**, 062509 (2007).

[66] R. D. Cowan, *The Theory of Atomic Structure and Spectra* (University of California Press, Berkeley, CA, 1981).

[67] W. J. Childs, L. S. Goodman, and V. Pfeufer, Phys. Rev. A **28**, 3402 (1983).

[68] W. G. Jin, T. Horuguchi, M. Wakasugi, and Y. Yoshizawa, J. Phys. Soc. Jpn. **59**, 3148 (1990).

[69] W. J. Childs, Phys. Rev. A **2**, 1692 (1970).

[70] J. J. McClelland, Phys. Rev. A **73**, 064502 (2006).

[71] J. J. McClelland and J. L. Hanssen, Phys. Rev. Lett. **96**, 143005 (2006).

[72] A. J. Berglund, S. A. Lee, and J. J. McClelland, Phys. Rev. A **76**, 053418 (2007).

[73] A. J. Berglund, James L. Hanssen, and Jabez J. McClelland, Phys. Rev. Lett. **100**, 113002 (2008).

[74] M. Lu, S. H. Youn, and B. L. Lev, Phys. Rev. Lett. **104**, 063001 (2010).

[75] C. I. Hancox, S. C. Doret, M. T. Hummon, L. Luo, and J. M. Doyle, Nature (London) **431**, 281 (2004).

[76] A. Yamaguchi, S. Uetake, D. Hashimoto, J. M. Doyle, and Y. Takahashi, Phys. Rev. Lett. **101**, 233002 (2008).

[77] Y. Takasu, K. Honda, K. Komori, T. Kuwamoto, M. Kumakura, Y. Takahashi, and T. Yabuzaki, Phys. Rev. Lett. **90**, 023003 (2003).

[78] T. Fukuhara, S. Sugawa, and Y. Takahashi, Phys. Rev. A **76**, 051604 (2007).

[79] A. Yamaguchi, S. Uetake, and Y. Takahashi, Appl. Phys. B **91**, 57 (2008).

[80] Y. Takasu and Y. Takahashi, J. Phys. Soc. Jpn. **78**, 012001 (2009).

[81] T. Fukuhara, S. Sugawa, Y. Takasu, and Y. Takahashi, Phys. Rev. A. **79**, 021601(R) (2009).

[82] V. A. Sautenkov, Y. V. Rostovtsev, H. Chen, P. Hsu, Girish S. Agarwal, and M. O. Scully, Phys. Rev. Lett. **94**, 233601 (2005).

[83] B. S. Ham, P. R. Hemmer, and M. S. Shahriar, Opt. Commun. **144**, 227 (1997).

[84] B. S. Ham, P. R. Hemmer, and M. S. Shahriar, Phys. Rev. A **59**, 2583(R) (1999).

[85] A. V. Turukhin, V. S. Sudarshanam, M. S. Shahriar, J. A. Musser, B. S. Ham, and P. R. Hemmer, Phys. Rev. Lett. **88**, 023602 (2001).

[86] J. Klein, F. Beil, and T. Halfmann, J. Phys. B **40**, 345 (2007).

[87] J. Klein, F. Beil, and T. Halfmann, Phys. Rev. Lett. **99**, 113003 (2007).

[88] J. Klein, F. Beil, and T. Halfmann, Phys. Rev. A **78**, 033416 (2008).

[89] S. W. Hell and J. Wichmann, Opt. Lett. **19**, 780 (1994).

[90] T. A. Klar, E. Engel, and S. W. Hell, Phys. Rev. E **64**, 066613 (2001).

[91] E. Betzig, Opt. Lett. **20**, 237 (1995).

[92] C. Hettich, C. Schmitt, J. Zitzmann, S. Kuhn, I. Gerhardt, and V. Sandoghdar, Science **298**, 385 (2002).

[93] A. N. Boto, P. Kok, D. S. Abrams, S. L. Braunstein, C. P. Williams, and J. P. Dowling, Phys. Rev. Lett. **85**, 2733 (2000).

[94] M. D'Angelo, M. V. Chekhova, and Y. Shih, Phys. Rev. Lett. **87**, 013602 (2001).

[95] K. S. Johnson, J. H. Thywissen, N. H. Dekker, K. K. Berggren, A. P. Chu, R. Younkin, and M. Prentiss, Science **280**, 1583 (1998).

[96] S. J. Bentley and R. W. Boyd, Opt. Express **12**, 5735 (2004).